Journal of Translational Medicine

RESEARCH

Open Access

Human collagen III mRNA therapy for effective skin rejuvenation

Jiamin Zhang[1†], Shuqi Chen[1†], Jiaqi Yang[1], Lianhao Song[1], Linfeng Chen[1], Wei Feng[1], Rong Ju[1] and Zhi Xie[1*]

Abstract

Background Skin photoaging leads to the deterioration of dermal collagen and overall skin integrity, resulting in visible signs of aging, particularly around the eye. Collagen III plays a pivotal role in maintaining skin elasticity and facilitating proper collagen fibril organization. Messenger RNA (mRNA)-based therapeutics present a novel alternative for addressing these limitations by enabling the localized production of full-length, biologically active proteins.

Methods This study evaluates the therapeutic effects of human collagen III (hCOL3A1) mRNA on UVB-induced skin photoaging using in *vitro* and in *vivo* models. In *vitro*, human fibroblasts were used to assess oxidative stress, senescence, apoptosis, proliferation, and migration. In *vivo*, a UVB-induced murine photoaging model was used to assess skin barrier function, dermal thickness, collagen content, and senescence markers were analyzed post-treatment. Transcriptome analysis was conducted to explore gene expression changes and key pathways involved in photoaging and repair mechanisms.

Results Our findings demonstrate that h*COL3A1* mRNA reduces oxidative stress, senescence, apoptosis and promotes cell proliferation and migration in a photoaging cell model. In a murine photoaging model, h*COL3A1* mRNA significantly improves skin barrier function, enhances dermal thickness, restores collagen content, improves dermal structure, and reduces cellular senescence markers without inducing systemic toxicity or immunogenicity. Transcriptome analyses reveal that h*COL3A1* mRNA reverses UVB-induced gene expression changes, reinstating critical signaling pathways for skin homeostasis and fibroblast function.

Conclusions These results highlight hCOL3A1 mRNA as a promising therapeutic candidate for skin photoaging and underscore the potential of mRNA-based therapies in dermatology and regenerative medicine.

Keywords Skin aging, UV irradiation, Collagen, mRNA therapy, Fibroblasts, Lipid nanoparticles, Dermatology

[†]Jiamin Zhang and Shuqi Chen contributed equally to this work.

*Correspondence:
Zhi Xie
zhi.xie@outlook.com
[1]State Key Laboratory of Ophthalmology, Zhongshan Ophthalmic Center, Guangdong Provincial Key Laboratory of Ophthalmology and Visual Science, Sun Yat-sen University, Guangzhou 510060, China

Introduction

Skin aging is a multifaceted process resulting from the interplay of intrinsic and extrinsic factors [1]. While intrinsic aging is largely determined by genetic and physiological changes over time, extrinsic aging arises mainly from environmental stressors. Among these, ultraviolet (UV) radiation is the most significant contributor to premature skin aging, a process commonly known as photoaging [2–4]. Cumulative UV exposure leads to DNA damage, impaired DNA synthesis and repair [5], inflammation [6], reactive oxygen species (ROS) generation [7] and the disruption of vital signaling pathways [8]. Clinically, these alterations manifest as fine lines, wrinkles, skin thickening, and a marked loss of elasticity [9–12]. Thus, the development of effective strategies to mitigate UVB-induced damage is imperative, particularly in vulnerable areas like the periorbital region.

Dermal fibroblasts are pivotal in maintaining the extracellular matrix (ECM) integrity, synthesizing its components—most notably collagen, proteoglycans, and growth factors [13, 14]. Collagen, particularly type I, constitutes about 75% of the dermis and provides structural support [15]. Type III collagen, often deemed "immature," is essential for skin elasticity and proper fibril formation [16–18]. Studies have shown that applying recombinant humanized collagen III can improve collagen content and enhance skin elasticity in animal models of UV-induced damage [19]. These findings highlight the therapeutic potential of collagen III for repairing and regenerating skin affected by photoaging.

Despite this promise, the commercial production and clinical use of collagen III face several limitations. Animal-derived products may cause immunogenicity, while recombinant proteins often lack full-length collagen and proper post-translational modifications [20–22]. Additionally, collagen's sensitivity to temperature and pH fluctuations complicates storage, increases costs, and necessitates frequent administrations [23, 24]. Retinoic acid (RA), another widely used treatment, promotes collagen synthesis but causes irritation, dryness, and UV sensitivity, leading to poor compliance [25–27]. These limitations highlight the need for alternative therapeutic strategies that can effectively restore collagen while minimizing side effects.

The emergence of mRNA-based therapeutics offers a promising alternative to these conventional protein-or small molecules therapies. Unlike DNA-based approaches, mRNA does not integrate into the host genome, mitigating risks of insertional mutagenesis [28]. Moreover, mRNA can be rapidly designed and produced at scale, enabling the encoding of full-length human proteins. By leveraging the eukaryotic post-translational machinery, mRNA-based therapeutics can yield proteins with high biological activity, circumventing many issues associated with recombinant collagen. This approach could allow the delivery of precise, full-length collagen III to targeted cells, enabling efficient treatments.

In this study, we investigated the therapeutic potential of mRNA of human collagen III (h*COL3A1*, Human Collagen Type III Alpha 1 Chain), delivered via lipid nanoparticles (LNPs), for treating UVB-induced skin photoaging. We demonstrate that hCOL3A1 mRNA stimulates collagen production, alleviates oxidative stress and senescence, and enhances skin structure in vitro and in vivo. The development of mRNA-based treatments may ultimately offer a safer, more adaptable, and patient-friendly alternative to current protein- or small molecules- based therapies, paving the way for personalized interventions in aesthetic medicine and dermatology.

Materials and methods

Preparation of mRNA and LNPs

Construction mRNA vectors

The reporter gene *FLUC*, as well as the gene of interest COL3A1 (GENE ID 1281) with a C-terminal FLAG tag, was cloned into a pUC57 vector containing a T7 promoter, which served as the DNA template for in *vitro* transcription. The recombinant plasmids were propagated in E.coli DH5α cells and purified using an EndoFree Plasmid Maxi Kit (Qiagen, Hilden, Germany). Following PCR amplification and agarose gel electrophoresis, DNA fragments were purified using the MinElute Gel Extraction Kit (Qiagen, Hilden, Germany). COL3A1 mRNA was synthesized using the T7 High-Yield RNA Synthesis Kit (New England Biolabs, Hitchin, UK), with UTP replaced by 1-methylpseudouridine triphosphate (N1-methylpseudouridine-5'-triphosphate, m1ΨTP) to enhance transcript stability. To further improve mRNA stability, the synthesized mRNA was capped with the m7G(5') ppp(5') RNA structure analog (New England Biolabs). After in *vitro* transcription, residual DNA was degraded using DNase I (New England Biolabs, Hitchin, UK). The integrity and molecular weight of the synthesized mRNA were confirmed by mass spectrometry, while purity and potential degradation products were analyzed by high-performance liquid chromatography (HPLC). For HPLC analysis, 2 μg of mRNA was loaded per run to verify transcript quality. All mRNAs were assessed by agarose gel electrophoresis and stored at -20 °C.

DsRNA ELISA

The sandwich enzyme-linked immunosorbent assay (sandwich ELISA) (Vazyme, Jiangsu, China, Cat. No.DD3509) was used to quantify dsRNA levels in in *vitro* synthesized mRNA following the manufacturer's instructions with modifications. Briefly, the capture antibody F2 (mouse IgG2a monoclonal antibody) was immobilized on microtiter plates to form a solid-phase

antibody. DsRNA standards and test samples were then added to the antibody-coated plates and incubated for 2 h at room temperature. After washing, the plates were incubated with the detection antibody M5 (purified mouse IgM monoclonal antibody) for 1 h at room temperature. Following another wash, the plates were further incubated with a horseradish peroxidase-conjugated secondary antibody for 1 h to form the 'capture antibody-antigen-enzyme-labeled detection antibody' complex. After the final wash, a colorimetric substrate was added for signal development, and the reaction was terminated. Absorbance was measured at 450 nm, with values directly correlating to dsRNA levels in the samples.

LNPs encapsulation of mRNA

LNPs were utilized for the encapsulation of mRNAs using the NanoAssemblr Ignite system, as described in the manufacturer's instructions. Briefly, an aqueous mRNA solution at pH 4.0 was rapidly mixed with a lipid mixture dissolved in ethanol. The lipid mixture consisted of the ionizable cationic lipid SM-102 (Sinopeg, #2089251-47-6), distearoylphosphatidylcholine (DSPC, Avanti, #850365P-1G, 18:0 PC), cholesterol (Sigma, #C8667-1G), and DMG-PEG2000 (Avanti, #880151P-1G) at a molar ratio of SM-102:DSPC: cholesterol: DMG-PEG2000 = 50:10:38.5:1.5. The concentration and encapsulation efficiency of the mRNAs were assessed using the Quant-iT RiboGreen RNA Assay Kit (Invitrogen, R11490). Additionally, the particle size and polydispersity index (PDI) of the LNP-mRNA complexes was measured using dynamic light scattering (DLS) with a Malvern Zetasizer Nano-ZS 300. The samples were exposed to a red laser, and the scattered light was detected. Data analysis was performed using Zetasizer V7.13 software to obtain the autocorrelation function. DLS measurements were performed exclusively to determine hydrodynamic particle size distribution and PDI, while encapsulation efficiency was calculated based on the RiboGreen assay. Representative DLS particle size distribution curves are provided in the Supplementary Figures (Fig. S1H).

In vitro experiments

Cell culture and drug treatment

The human fibroblast cell line HFF-1 was obtained from the Cell Bank/Stem Cell Bank, Chinese Academy of Sciences (Shanghai, China). Cells were cultured in Dulbecco's modified Eagle's medium (DMEM) supplemented with 10% FBS, 2mM glutamine, 100U/mL penicillin, and 100 μg/mL streptomycin at 37 °C in a humidified atmosphere of 5% CO_2. RA (MCE, New Jersey, USA) was used as a positive control therapy due to its well-documented effects in promoting collagen synthesis, enhancing extracellular matrix remodeling, and reducing photoaging-associated damage. RA exerts its function by binding to nuclear retinoic acid receptors (RARs), thereby regulating the transcription of target genes involved in cell proliferation, differentiation, and collagen metabolism. RA was dissolved in DMSO at a concentration of 10mM and stored at − 20 °C. The treatment was applied 6 h prior to UVB irradiation. The RA therapeutic concentration was 2μM, 6 h prior to UVB irradiation.

For in *vitro* mRNA transfection, h*COL3A1* mRNA was transfected into HFF-1 cells using Lipofectamine™ MessengerMAX™ (Thermo Fisher Scientific, Waltham, MA, USA), according to the manufacturer's instructions. For 24-well plates ($0.5–2 \times 10^5$ cells/well), 500 ng of hCOL3A1 mRNA was diluted in 25 μL Opti-MEM™, and 0.75 μL Lipofectamine™ MessengerMAX™ was diluted in 25 μL Opti-MEM™ and incubated 10 min. The mRNA and reagent were then combined and incubated 5 min to form complexes, which were added to cells (50 μL/well). Cells were incubated under standard conditions for 6 h prior to UVB irradiation. Volumes were scaled proportionally for 96- and 6-well plates.

Cell photoaging model establishment

HFF-1 cells were washed twice with 1×PBS prior to UVB irradiation and then covered with a thin film of PBS during exposure. A battery of TL20W fluorescent tubes (Philips, Amsterdam, Netherlands) was used as the UVB source, with a wavelength range of 305–315 nm, peaking at 311 nm. Cells were exposed to bi-daily UVB irradiation over two consecutive days, totaling three rounds of irradiation, followed by a 24-hour incubation in culture medium (Fig. S2A). UVB irradiation induced senescence-associated phenotypes in HFF-1 cells, marked by reduced cell density and disorganized morphology (Fig. S2B). Cell viability was assessed 24 h after irradiation to determine the optimal dose that would induce damage without causing extensive cell death. Cell viability began to decline at 50 mJ/cm², with microscopic evidence of cell death observed as energy levels increased. At 50 mJ/cm², cell viability fell below 50%, representing the half-lethal dose. This threshold was selected as the experimental condition to evaluate the protective effects and mechanisms of potential interventions under significant yet sublethal stress. Based on these findings, 50 mJ/cm² was identified as the optimal irradiation dose for subsequent experiments. The duration of UVB exposure required to achieve 50 mJ/cm² was approximately 667 s (≈11 min), based on the measured UVB lamp irradiance of 75 uW/cm². The dose was calculated using Dose (mJ/cm²) = Irradiance (mW/cm²) × Time (s). Moreover, the pre-treatment group with h*COL3A1* mRNA exhibited higher cell viability compared to the post-treatment group under UVB irradiation at varying doses ($p < 0.001$ at 50 mJ/cm²) (Fig. S2C and D). HFF-1 cells were cultured in complete medium at 37 °C for 24 h under 5% CO_2.

Cell proliferation analysis

The plate was imaged using a 10× objective on the Operetta CLS™ high-content analysis system (PerkinElmer, UK), capturing nine fields of view per well. Cell counts were quantified using a custom assay developed in the Custom Module Editor. Cell viability was calculated as the ratio of healthy viable cells at each time point in each treatment group to the healthy viable cells in the control group at the corresponding time point. Each group included six replicates.

Cell migration assay

Cells were seeded in a 6-well plate and subjected to UVB modeling. A scratch was made in the cell monolayer using a 200μL pipette tip following the treatment. The culture plate was incubated at 37 °C in a 10× objective on the Operetta CLS™ high-content analysis system (PerkinElmer, UK) under 5% CO_2 and 95% air conditions. Images were captured from nine fields of view at 0, 12, and 24 h post-scratching, and the open area of the scratch was analyzed using the software's measurement tools. Each group included three replicates.

SA-β-Gal staining

SA-β-Gal staining was conducted using the Senescence-β-Galactosidase Staining Kit (Abcam, MA, USA), following the manufacturer's instructions. Briefly, cells were washed with 1×PBS and fixed for 15 min. Following this, cells were washed twice with 1×PBS and incubated with SA-β-Gal Staining Solution overnight at 37℃ in a dry incubator without CO_2. Cells were washed and counterstained with 1 μg/mL DAPI (Sigma-Aldrich, Saint Louis, USA) for 5 min, then observed under 20× magnification. The percentage of positive cells was calculated by counting cells in 3 random fields.

Detection of ROS

Intracellular ROS were detected using the DCFH-DA fluorescence assay. DCFH-DA was dissolved in DMSO at a concentration of 10mM and stored at -20℃. DCFH-DA solution (DCFH-DA: serum-free medium, 1:1000) was added to each well at the specified time points. After incubation for 10 min, cells were washed three times with serum-free medium. Images were captured using an inverted fluorescence microscope. The fluorescence intensity of intracellular ROS was quantitatively measured using a fluorescent microplate reader (excitation: 485 nm, emission: 525 nm).

Note RA was not included in the ROS assay because the focus of this experiment was to evaluate the direct effect of hCOL3A1 mRNA on UVB-induced oxidative stress. The protective effects of RA have been previously established in other cellular assays and thus were not repeated here to reduce experimental redundancy.

RNA isolation and quantitative real-time PCR (RT-qPCR)

Total RNA was extracted using TRIzol. RNA was converted to cDNA using the HiScript III RT SuperMix for RT-qPCR (Vazyme, Jiangsu, China). RT-qPCR was conducted using the LightCycler® 480 Instrument II (Roche, Basel, Switzerland) with iTaqTM Universal SYBR® Green Supermix (Bio-Rad, Hercules, California), according to the manufacturer's protocol. The relative expression level was calculated using the $2^{-}\boldsymbol{\Delta\Delta Ct}$ method. The primers are listed in the Supplementary To distinguish between exogenous and endogenous mRNA, specific primers were designed for endogenous transcripts. All primer sequences are listed in the Supplementary Table 1.

Western blot analysis

Total protein was extracted from cells using RIPA buffer and quantified using a BCA kit. Protein samples were separated by 10% sodium dodecyl sulfate-polyacrylamide gel electrophoresis (SDS-PAGE) and transferred to 0.2 μm PVDF membranes (Millipore, MA, USA). Non-specific binding was blocked with 5% skim milk for 1 h. The membrane was incubated overnight at 4 °C with each primary antibody targeting specific proteins, including anti-p21 (CST, 1:1000 dilution), anti-Flag (CST, 1:1000 dilution), anti-collagen III (Abcma, 1:1000 dilution), and anti-β-actin (Proteintech, 1:20000 dilution). The membrane was then incubated for 1 h with a secondary antibody, goat anti-rabbit IgG, and goat anti-mouse IgG conjugated to HRP. Chemiluminescence was detected using an ECL kit (SmartBuffers, Femto-Sensitive ECL Solution, China).

In vivo experiments

Animals

Animal experiments were conducted with approval from the Institutional Animal Care and Use Committee (IACUC) of Zhongshan Ophthalmic Center, Sun Yat-Sen University (Approval No. Z2023009). In vivo experiments were performed using 8-week-old female Balb/c-nude mice.

Photoaging mice models establishment

Establishing the skin-photoaging model involved subjecting female nude mice (6–8 weeks old) to UVB irradiation on their dorsal skin every other day for 8 weeks using a Philips UV lamp emitting at a wavelength of 311 nm. As shown in the diagram, the UVB irradiation source was positioned approximately 30 cm above the Balb/c-nude mice confined in the box, allowing them to move freely (Fig. S3A). The UV irradiation protocol started at

an initial intensity equivalent to the minimal erythemal dose (MED) of 1 MED (60 mJ/cm²) for the first 2 weeks. The intensity was then gradually increased to 2 MED (120 mJ/cm²) in the third week, 3 MED (180 mJ/cm²) in the fourth week, and maintained at 4 MED (240 mJ/cm²) from the fifth to eighth week of the experiment. The total UVB dose delivered over the 8 weeks approximated 80 MED. Irradiation was administered until visible wrinkles appeared on the dorsal skin of the mice, after which the experiment proceeded(Fig. S3B). Following the 8-week irradiation regimen, the nude mice were randomly assigned to one of three treatment groups (eight mice per group): (1) Vehicle control (UVB irradiation + empty-hCOL3A1 mRNA-LNP), (2) Positive control (UVB irradiation + 0.05% RA), (3) UVB irradiation + h*COL3A1* mRNA-LNP administered via intradermal injection using 33G insulin needle. Skin treatments were performed on days 1, 4, 7, 14, and 21. Skin tissue was collected on days 28.

For in *vivo* experiments, 500 ng hCOL3A1 mRNA per injection site was delivered intradermally into mice five times, following preliminary optimization studies. All in *vitro* and in *vivo* treatments used equivalent dosing relative to cell number or tissue volume to ensure consistency across experiments.

Hydroxyproline (HYP) content detection

Following the manufacturer's instructions, total collagen content was quantified using a HYP assay kit (Solarbio, Beijing, China). Skin tissue was cut into pieces and fully hydrolyzed via acid hydrolysis at 110 °C for 6 h. The solution was neutralized with NaOH and centrifuged at 16,000 rpm at 25 °C for 20 min. Absorbance was measured at 560 nm. Standard curves were generated using a standard solution supplied by the manufacturer.

HE staining

The tissue sections were passed through a series of decreasing alcohol concentrations to remove xylene and thoroughly rinsed in water. The sections were stained with hematoxylin for 2 min and treated with acidic alcohol differentiation. After staining with eosin for 2 min and dehydrating with ethanol, the sections were cleared with xylene and mounted.

Masson staining

For Masson staining, sections were deparaffinized, rehydrated, and incubated in hematoxylin iron solution for 3 min. After differentiation using 0.5% hydrochloric acid ethanol, acid fuchsin solution was applied for 10 min. This was followed by treatment with 1% phosphomolybdic acid in water for approximately 3 min and direct staining with aniline blue solution for an additional 6 min. Subsequently, the sections were treated with 1% glacial acetic acid for 1 min. The sections were mounted using xylene, followed by neutral gum.

Sirius red staining

The paraffin sections were rehydrated and stained with Sirius red for 8 min. The sections were visualized under polarized light. Type I collagen appears as orange or bright red coarse fibers, while collagen III appears as green fine fibers.

Immunohistochemical staining and analysis

Skin sections were deparaffinized in xylene, followed by dehydration through graded ethanol, and washed three times with PBS for 5 min. After blocking with 3% (w/v) H_2O_2 for 15 min, the sections were blocked with 1% BSA in TBST for 1 h at room temperature. A specific primary antibody against p16 (ABclonal, 1:200 dilution) was incubated with the tissue sections overnight. After three washes in PBS, the sections were incubated with the MaxVision™ HRP-Polymer anti-Mouse/Rabbit IHC Kit (Maixin Biotech, Fuzhou, China) for 15 min. The chromogenic substrate used was the AEC Kit (20×) (Maixin Biotech, Fuzhou, China), and hematoxylin was used as the counterstain. The number of positive cells in each visual field was calculated as follows: (number of positive cells / total cells) × 100%.

TEWL test

The TEWL was measured using the DermaLab Combo system (Cortex Technology, Hadsund, Denmark) from the dorsal skin of the mice. A probe placed on the skin was stabilized for approximately 30 s, with each measurement taken eight times and averaged. Measurements were conducted before and after treatment at room temperature (21 °C to 22 °C) and relative humidity (50% to 55%).

Safety evaluation

Luminescence in vivo imaging

FLUC mRNA-intradermal-treated mice were imaged using an in vivo imaging system (NightOWL LB 983, Berthold, Germany) on days 1, 2, 3, 5, and 7. The parameters were set as follows: luminescence exposure time of 60 s, photo exposure time of 0.1 s, and a sample size of 120 × 120 field of view for the specified luminescence imaging times. Quantitative analysis of intensity was performed by measuring the total (cps) signal within a region of interest. Images were analyzed using Indigo Imaging Software Ver. A 01.19.01.

Assessment of hepatic function in mice

Mice received intradermal injections of h*COL3A1* mRNA five times. Blood samples were collected via the eyeball at room temperature, rather than via the tail vein,

to allow the collection of larger blood volumes necessary for multiple biochemical assays, including ALT, AST, ALB, TBIL-Z, and ALP. Samples were then centrifuged at 2000 rpm for 15 min at 4 °C. The resulting supernatant was analyzed using an automatic biochemical analyzer (BK-280, BIOBASE, China) according to the manufacturer's instructions for ALT, AST, ALB, TBIL-Z, and ALP kits (BK-280, BIOBASE, China).

Inflammasome protein measurements

Inflammasome signaling protein levels (IL-6 and TNF-α) in cell culture medium were analyzed as described in reference [29] using the Ella System and analyzed with Simple Plex Explorer software (ProteinSimple). Results represent the mean of triplicate samples for each analyte.

Transcriptome analysis

Library preparation for RNA sequencing

2 μg of RNA per sample was used as input material for RNA sample preparations. Sequencing libraries were generated using the NEBNext® UltraTM RNA Library Prep Kit for Illumina® (#E7530L, NEB, USA), following the manufacturer's instructions. Index codes were added to link sequences to individual samples. Briefly, mRNA was purified from total RNA using poly-T oligo-attached magnetic beads. Fragmentation was carried out using divalent cations under elevated temperature in NEBNext First Strand Synthesis Reaction Buffer (5X). First-strand cDNA was synthesized using a random hexamer primer and RNase H, followed by second-strand cDNA synthesis with buffer, dNTPs, DNA polymerase I, and RNase H. Library fragments were purified using QIAquick PCR kits, eluted with EB buffer, and subjected to terminal repair, A-tailing, and adapter addition. PCR amplification was performed to enrich the library products.

Library clustering and sequencing

Library clustering and sequencing were conducted as follows: index-coded sample clustering was performed using a cBot cluster generation system with the HiSeq PE Cluster Kit v4-cBot-HS (Illumina) in accordance with the manufacturer's instructions. Following cluster generation, the libraries were sequenced on an Illumina platform, producing 150 bp paired-end reads.

Bioinformatical analysis

RNA-seq raw data were preprocessed and quality-controlled using fastp (v0.23.4) [30]. The mouse rRNA reference sequence file was downloaded from NCBI (GRCm39, GCF_000001635.27,https://ftp.ncbi.nlm.nih.gov/genomes/all/GCF/000/001/635/GCF_000001635.27_GRCm39/GCF_000001635.27_GRCm39_rna_from_genomic.fna.gz). rRNA reference index was constructed and local alignment was performed by Bowtie2 (v2.5.4). Reads aligned to the rRNA reference sequence were filtered out [31]. The mouse genome reference sequence and gene annotation file were obtained from Ensembl (GRCm39 Ensembl Release 111, DNA sequence: https://ftp.ensembl.org/pub/release111/fasta/mus_musculus/dna/Mus_musculus.GRCm39.dna_sm.primary_assembly.fa.gz, Gene annotation: https://ftp.ensembl.org/pub/release111/gtf/mus_musculus/Mus_musculus.GRCm39.113.gtf.gz). Mouse reference index was built and aligned using STAR (v2.7.11b), and gene expression was quantified via RSEM (v1.3.3). Gene expression matrices were normalized [32, 33], and differentially expressed genes were identified using DESeq2 (v1.44.0)within R (version 4.4.1) [34]. KEGG and GOBP enrichment analyses were conducted using fGSEA (v1.30.0) [35].

Statistical analysis

Statistical analyses were performed using GraphPad Prism 9.5. A significance threshold of $p < 0.05$ was applied. Data are expressed as mean ± SEM. Unpaired Student's t-test was used for statistical comparisons between two groups, and ANOVA with Tukey's post hoc was used between multiple groups.

Results

Preparation, Synthesis, and delivery of h*COL3A1* mRNA

To explore a potential therapeutic intervention for UVB-induced skin photoaging, we designed and synthesized a full-length h*COL3A1* mRNA and encapsulated it in LNPs for delivery. Agarose gel electrophoresis revealed a distinct band corresponding to the expected full size of the h*COL3A1* and firefly luciferase (*FLUC)* mRNA (Fig. S1A and B), and the complete sequences have been provided in the Supplementary Tables (2–4). To further evaluate the capping efficiency of in *vitro* transcribed (IVT) mRNA, we quantified it using high-sensitivity mass spectrometry analysis. The results indicate that 99.95% of the mRNA is successfully capped, with only 0.05% remaining as uncapped 5'-triphosphate RNA(Fig. S1C). HPLC analysis exhibited a single, sharp peak, indicating that the purified mRNA was of high quality (Fig. S1D). Additionally, the dsRNA concentration analysis revealed that the dsRNA content in *FLUC* mRNA was 0.120%, whereas in hCOL3A1 mRNA, it was 0.097%, which is well below the threshold required to significantly activate the TLR3/RIG-I/MDA5 pathways and induce an immune response (Fig. S1E and F).

We first examined the in vitro expression of the introduced h*COL3A1* mRNA in human fibroblast cells (HFF-1). Immunofluorescence detection of FLAG-tagged COL3A1 proteins showed positive signals at 6 h post-transfection, which persisted through 24 h (Fig. 1A and B). To enable effective delivery in vivo, we encapsulated the mRNA within LNPs. DLS confirmed that the

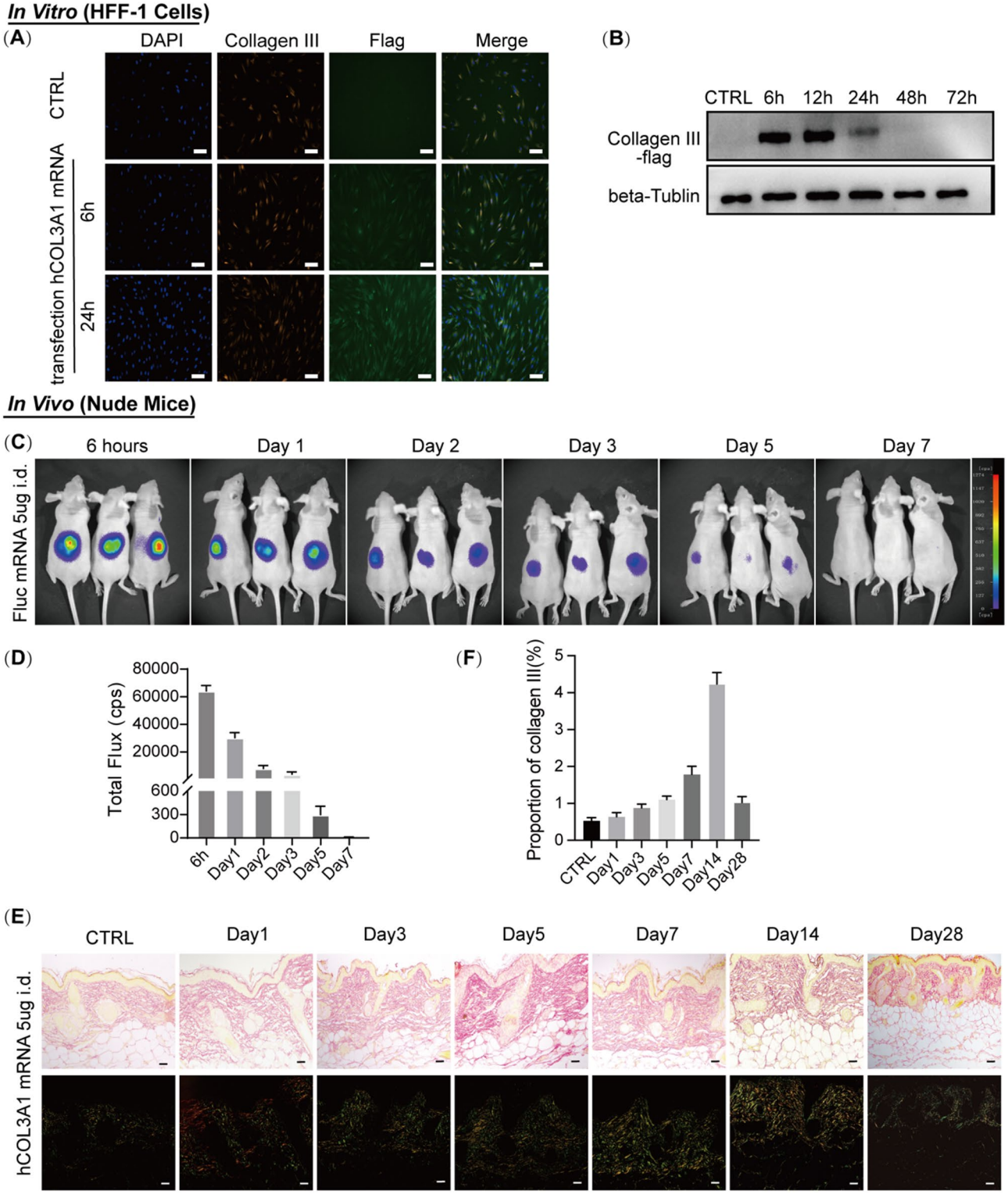

Fig. 1 Synthetic mRNA delivery and protein expression in vitro and in vivo. (**A**) Representative images showing total Collagen III protein (red) and exogenous hCOL3A1 protein tagged with FLAG (green) in HFF-1 cells transfected with h*COL3A1* mRNA, captured at time points ranging from 6 to 24 h. Scale bar: 75 μm. (**B**) Western blot analysis of exogenous hCOL3A1 protein in HFF-1 cells transfected with h*COL3A1* mRNA. β-tubulin was used as a loading control. (**C**) Representative images showing Fluc protein expression in mice following intradermal (i.d.) injection of 5 μg *FLUC* mRNA-LNP at different time points. (**D**) Quantification of *FLUC* protein expression after intradermal *FLUC* mRNA-LNP injection ($n = 3$). Data are presented as mean ± SEM. (**E**) Representative Picro-Sirius Red staining images showing total COL3A1 protein expression in mice following intradermal injection of 5 μg h*COL3A1* mRNA-LNP at different time points. Vehicle injection served as a sham control. Scale bar: 50 μm. (**F**) Quantification of total Collagen III protein expression in (**E**) after intradermal h*COL3A1* mRNA-LNP injection ($n = 5$). Data are presented as mean ± SEM

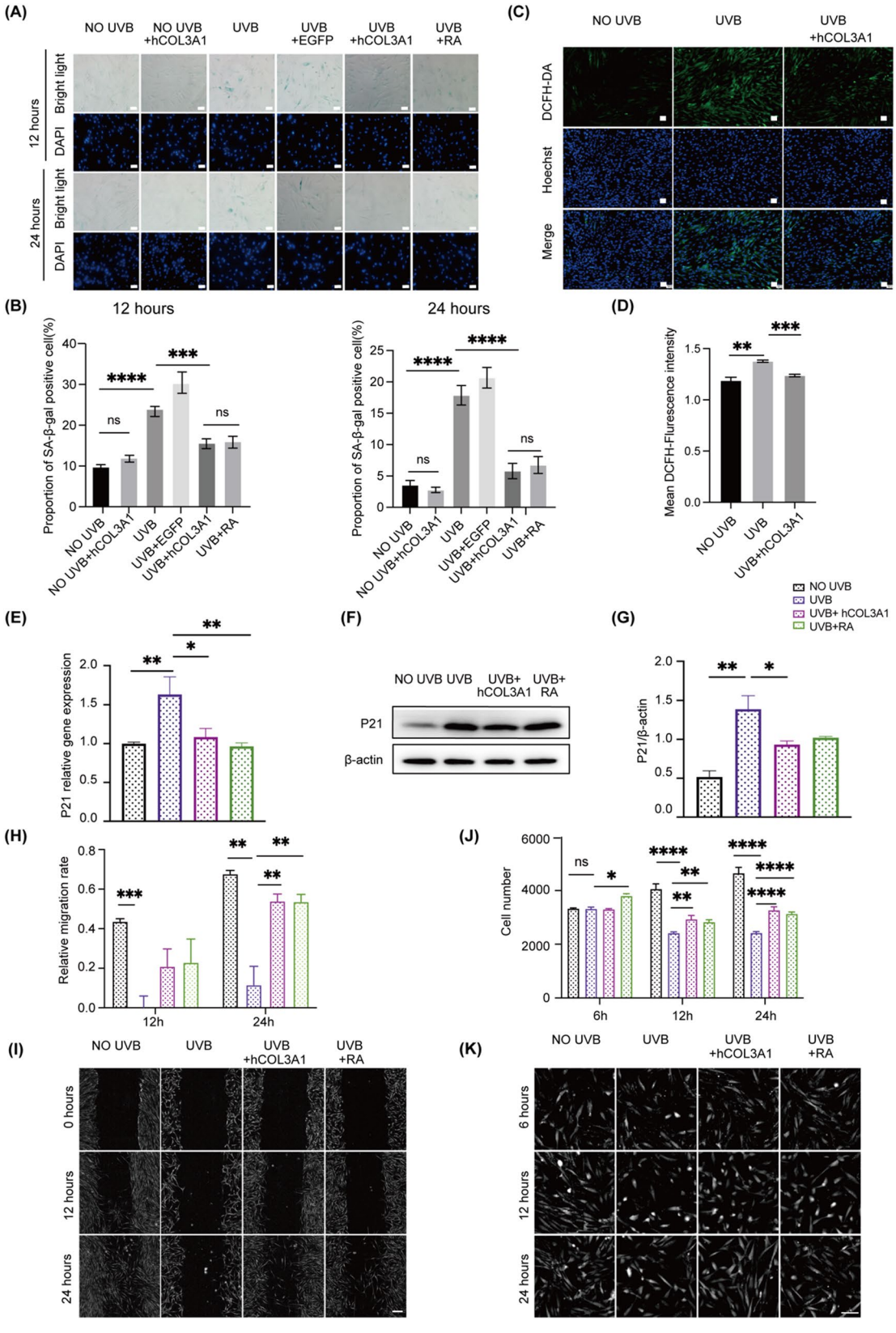

Fig. 2 (See legend on next page.)

(See figure on previous page.)

Fig. 2 h*COL3A1* mRNA Reduces Senescence and Apoptosis, and Promotes Cell Proliferation and Migration. (**A**) Representative SA-β-gal staining images of HFF-1 cells after different treatments following UVB irradiation at different time points. Scale bar: 20 μm. (**B**) Quantification of (A), showing the proportion of SA-β-gal-positive cells. Data are presented as mean ± SEM ($n = 5$). (**C**) Representative fluorescence images showing ROS generation in HFF-1 cells after UVB irradiation and the rescue of ROS damage following h*COL3A1* mRNA treatment at different time points. Scale bar: 20 μm. (**D**) Quantification of ROS-positive green fluorescence intensity in HFF-1 cells after h*COL3A1* mRNA treatment following UVB irradiation. Data are presented as mean ± SEM ($n = 4$). (**E**) RT-qPCR analysis of *P21* relative gene expression levels in HFF-1 cells after different treatments following UVB irradiation. Data are presented as mean ± SEM ($n = 5$). Each RT-qPCR assay was performed in triplicate. (**F**) Western blot analysis of P21 protein levels in HFF-1 cells after different treatments following UVB irradiation. β-actin was used as a loading control. (**G**) Quantification of P21 protein levels from Western blot bands in (**F**). (**H**) Quantitative analysis of scratch assay and fusion rates of HFF-1 cells after different treatments following UVB irradiation at different time points. Data are presented as mean ± SEM ($n = 3$). (**I**) Representative images of HFF-1 cells following different treatments and UVB irradiation at different time points, captured from nine non-overlapping adjacent visual fields. Scale bar: 20 μm. (**J**) Quantitative analysis of HFF-1 cell viability following different treatments and UVB irradiation at different time points. Data are presented as mean ± SEM ($n = 6$). (**K**) Representative images of HFF-1 cell morphology following different treatments and UVB irradiation at different time points. Scale bar: 10 μm. Note: $^{*}p < 0.05$, $^{**}p < 0.01$, $^{***}p < 0.001$, $^{****}p < 0.0001$, ns = not significant, determined by one-way analysis of variance (ANOVA)

particles had a mean diameter of 84.41 ± 1.458 nm with a PDI of 0.15, indicating good homogeneity (Fig. S1G -H) [36–40]. To test intradermal delivery of mRNA-LNP formulation Fand its in vivo expression, we injected *FLUC* mRNA encapsulated by LNPs into the dorsal skin of mice and monitored bioluminescence over 7 days (Fig. 1C). The luminescence peaked at 6 h post-injection, gradually declining to near-background levels by day 7 (Fig. 1D). These data confirmed that mRNA-LNP can be efficiently delivered and transiently expressed in skin.

We next assessed the conversion of h*COL3A1* mRNA into functional collagen III protein in vivo. Following intradermal injection of h*COL3A1* mRNA-LNP, Sirius Red staining of dorsal skin indicated a significant increase in collagen III content 24 h post-injection. Elevated collagen III levels were maintained for up to 28 days, consistent with prior studies [41, 42]. showing that collagen III in skin can persist for about four weeks before degradation (Fig. 1E and F).

Taken together, these results establish the successful synthesis of full-length h*COL3A1* mRNA, its encapsulation within LNPs, and its capability to drive robust collagen III protein production both in cultured fibroblasts and in mouse skin.

h*COL3A1* mRNA protects fibroblasts from UVB-Induced damage and restores function

Having confirmed effective delivery and expression of h*COL3A1* mRNA, we next investigated its protective effects against UVB-induced cellular damage in human fibroblasts [43]. Enhanced green fluorescent protein (EGFP) mRNA was served as a non-specific mRNA control, and RA was used as a positive control [44]. After UVB irradiation, senescence-associated β-galactosidase (SA-β-Gal) staining revealed a marked increase in senescent cells at both 12 and 24 h compared to non-irradiated controls ($p < 0.0001$) (Fig. 2A and B). In contrast, treatment with h*COL3A1* mRNA or RA significantly reduced SA-β-Gal positivity($p<0.01$ at 12 h and $p<0.0001$ at 24 h), indicating that h*COL3A1* mRNA can mitigate UVB-induced cellular senescence, as effectively as RA.

It is known that excessive UVB-induced ROS can cause oxidative damage, and excess cellular levels of ROS lead to activation of cell death processes such as apoptosis [45–48]. We found that UVB irradiation sharply increased intracellular ROS production, whereas h*COL3A1* mRNA treatment effectively lowered ROS levels ($p<0.01$) (Fig. 2C and D). In parallel, the expression of *CDKN1A* (*P21*), a cell cycle regulator often linked to senescence and apoptosis [49], was notably upregulated following UVB irradiation ($p<0.05$). In contrast, h*COL3A1* mRNA and RA both significantly suppressed *P21* activation($p<0.05$ and $p<0.01$), reinforcing the notion that h*COL3A1* mRNA helps maintain cellular homeostasis under photoaging stress (Fig. 2E-G).

We then assessed whether h*COL3A1* mRNA could promote cell motility. In a wound healing assay, UVB impaired fibroblast migration, whereas hCOL3A1 mRNA and RA significantly restored cell motility at 24 h ($p<0.01$ and $p<0.01$)(Fig. 2H and I). Additionally, UVB significantly reduced cell numbers at 12 and 24 h, while hCOL3A1 mRNA or RA treatment rescued viability, with stronger effects observed for hCOL3A1 ($p<0.01$ for h*COL3A1* and $p<0.05$ for RA at 12 h and $p<0.0001$ for h*COL3A1* and $p<0.001$ for RA at 24 h) (Fig. 2J and K).

In summary, h*COL3A1* mRNA exerts robust cytoprotective effects against UVB-induced photoaging in vitro. It reduces senescence and apoptosis, and promotes cell proliferation and migration, thereby highlighting its therapeutic potential for managing photoaging-induced dermal damage.

h*COL3A1* mRNA reverses UVB-induced skin damage in a mouse model

Encouraged by the in vitro results, we evaluated the therapeutic efficacy of h*COL3A1* mRNA in a UVB-induced photoaging mouse model (Fig. 3A). Chronic UVB irradiation led to visible signs of skin damage, characterized by persistent redness, roughness, and dryness of the dorsal skin (Fig. 3B). Following intradermal administration, hCOL3A1 mRNA-treated mice displayed smoother skin and reduced scaling compared to vehicle controls,

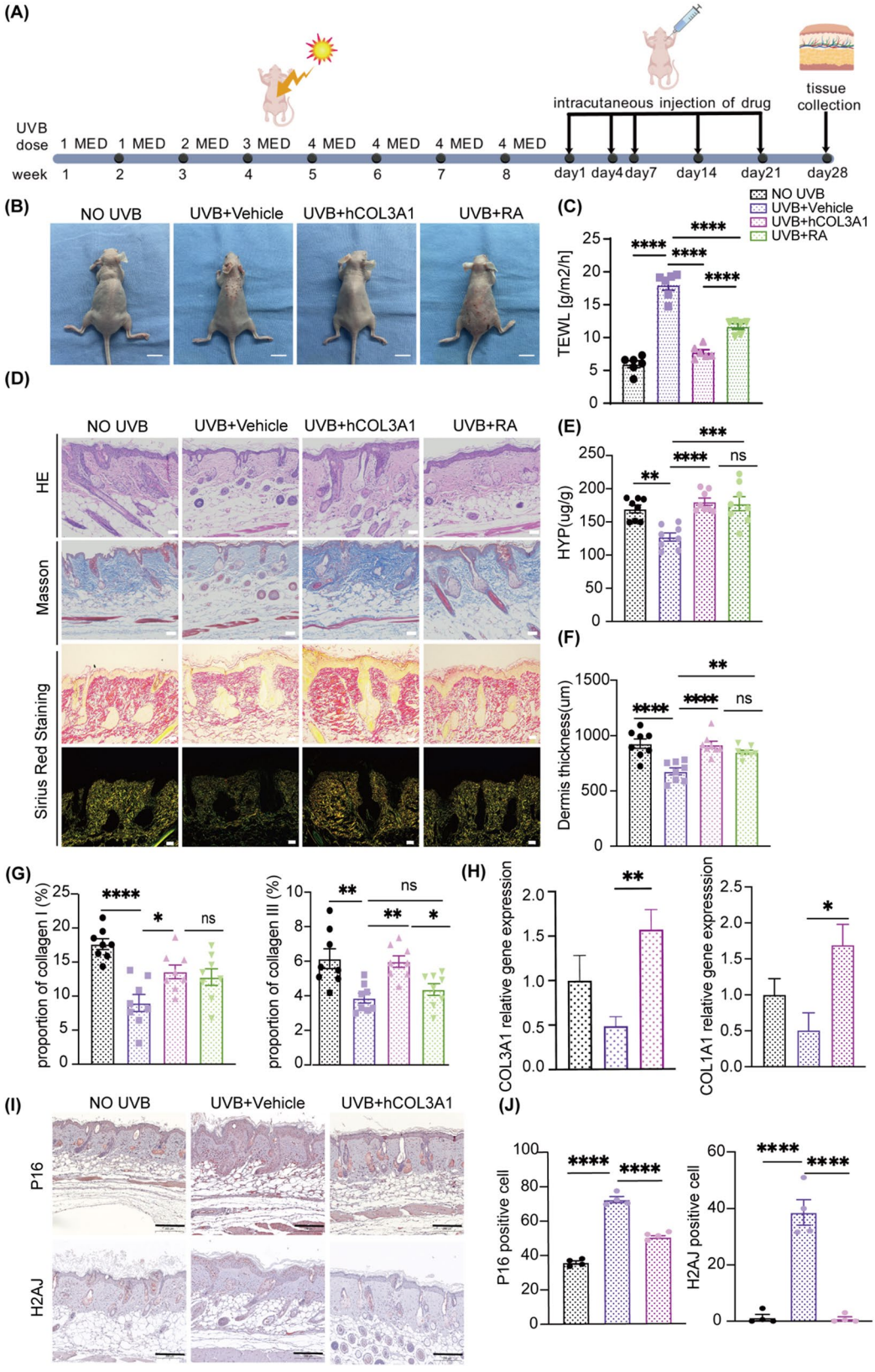

Fig. 3 (See legend on next page.)

(See figure on previous page.)

Fig. 3 The Therapeutic Efficacy of h*COL3A1* mRNA in a UVB-Induced Photoaging Mouse Model. (**A**) Schematic diagram illustrating the design of the animal experiments and timeline of five times injections of hCOL3Al mRNA. Skin tissue was collected at 28 days; 1MED = 60 mJ/cm^2. (**B**) Representative images of dorsal skin across different treatment groups. (**C**) Quantification of TEWL in dorsal skin following intradermal injection of different treatments after UVB irradiation. Data are presented as mean ± SEM ($n = 6$) with each TEWL measurement repeated eight times per mouse. (**D**) Representative images of dorsal skin stained with H&E, Masson, and Picro-Sirius Red following intradermal injection of different treatments after UVB irradiation. Scale bar: 50 μm. (**E**) HYP assay quantifying total collagen deposition in dorsal skin after different treatments following UVB irradiation. Data are presented as mean ± SEM ($n = 8$). (**F**) Quantification of dermal thickness based on Masson staining from (**D**). Data are presented as mean ± SEM ($n = 8$), derived from five non-overlapping visual fields per sample. (**G**) Quantification of collagen I and collagen III proportions from Picro-Sirius Red staining in (**D**). Data are presented as mean ± SEM ($n = 8$), derived from five non-overlapping visual fields per sample. (**H**) RT-qPCR analysis of *COL3A1* and *COL1A1* relative gene expression levels following h*COL3A1* mRNA treatment after UVB irradiation. Data are presented as mean ± SEM ($n = 3$). (**I**) Representative immunohistochemistry images of dorsal skin showing P16 and H2AJ expression across different treatment groups following h*COL3A1* mRNA treatment after UVB irradiation. Scale bar: 200 μm. (**J**) Quantification of the number of P16 and H2AJ-positive cells in (**I**). Data are presented as mean ± SEM ($n = 4$), derived from five non-overlapping visual fields per sample. Note: *$p < 0.05$, **$p < 0.01$, ***$p < 0.001$, ***$p < 0.0001$, ns = not significant, determined by one-way analysis of variance (ANOVA)

whereas RA produced milder improvements and induced skin redness, consistent with previous reports [25] (Fig. 3B). In contrast, the UVB + Vehicle group showed no amelioration of photoaging-related changes (Fig. 3B).

To gauge changes in skin barrier function, we measured trans-epidermal water loss (TEWL), a key indicator of barrier integrity [50]. While UVB exposure significantly increased TEWL, reflecting a compromised barrier ($p<0.0001$, unpaired t-test) (Fig. S3C and D). Both h*COL3A1* mRNA and RA treatments markedly reduced TEWL levels compared to the vehicle group ($p<0.0001$ and $p<0.0001$), restoring barrier function closer to that of non-irradiated skin. Notably, the h*COL3A1* mRNA group significantly reduced TEWL levels compared to the RA group ($p < 0.0001$) (Fig. 3C), indicating that h*COL3A1* mRNA therapy was more effective in preserving epidermal barrier function than RA therapy.

Histological assessments provided further evidence of therapeutic efficacy. Hematoxylin-eosin (H&E) and Masson's trichrome staining revealed that UVB irradiation caused dermal thinning and disrupted collagen fibers, resulting in disorganized and fragmented ECM structures. In mice treated with h*COL3A1* mRNA or RA, these pathological changes were substantially mitigated, with more orderly collagen fiber alignment and improved overall dermal architecture (Fig. 3D). Quantitative assays supported these histological findings. A HYP assay showed reduced total collagen content in vehicle-injected UVB model controls, whereas h*COL3A1* mRNA or RA administration significantly restored total collagen ($p < 0.0001$ and $p < 0.001$) (Fig. 3E). Quantification of dermis thickness in the tissues by Masson staining showed a decrease in total collagen levels and the h*COL3A1* mRNA and RA treatment significantly restored dermal thickness compared to the UVB + vehicle controls ($p < 0.0001$ for h*COL3A1* and $p < 0.01$ for RA) (Fig. 3F). Sirius Red staining further confirmed that h*COL3A1* mRNA treatment increased type I collagen levels ($p < 0.05$). Profoundly, h*COL3A1* mRNA also significantly increased the collagen III level while RA had no such effect ($p < 0.01$ for h*COL3A1* and $p > 0.05$ for RA) (Fig. 3G). Consistent with these results, RT-qPCR analysis of skin tissue revealed upregulation of collagen synthesis genes by the h*COL3A1* mRNA treatment, including *COL1A1* and *COL3A1* ($p<0.05$ and $p<0.05$) (Fig. 3H).

To assess the dosage effect of hCOL3A1 mRNA treatment, we evaluated both 500 ng and 5 μg dosages. Both 500 ng and 5 μg dosages significantly restored dermal thickness and collagen I + III levels after UVB exposure, with no difference between the two groups (Fig. S4A and B). Furthermore, results from both Masson staining and Sirius Red staining showed no statistically significant differences between the UVB + Vehicle group and the UVB + *FLUC* group, indicating that *FLUC* mRNA had no functional effect. Based on these findings, we conclude that the observed effects in the animal photoaging model were specifically attributed to our functional h*COL3A1* mRNA.

Finally, immunohistochemical staining for senescence markers p16INK4a and H2A.J [51, 52], which are well-established markers of cellular senescence, demonstrated higher expression in UVB-exposed vehicle controls. Intradermal injection of h*COL3A1* mRNA significantly reduced these senescence markers, indicating diminished cellular senescence and improved tissue homeostasis ($p<0.0001$, respectively) (Fig. 3I and J).

Overall, these findings show that h*COL3A1* mRNA injections effectively counteract UVB-induced skin photoaging in vivo. By improving barrier function, increasing collagen content and dermal thickness, and reducing cellular senescence, h*COL3A1* mRNA treatment holds promise as a therapeutic intervention for photoaged skin.

Transcriptome analysis of the protective effects of h*COL3A1* mRNA

To elucidate the molecular mechanisms underlying the protective effects of h*COL3A1* mRNA, we performed transcriptome analysis on dermal tissues harvested from three groups: the control group without UVB treatment (no UVB), vehicle-injection of UVB-exposed mice (UVB + vehicle), and h*COL3A1* mRNA-injection of UVB-exposed mice (UVB + h*COL3A1*). Compared with the no UVB control, the UVB + vehicle group exhibited 213 upregulated and 279 downregulated genes, indicating

substantial alterations in gene expression associated with photoaging-induced dermal damage (Fig. 4A). In contrast, the h*COL3A1* mRNA treatment showed 443 upregulated and 133 downregulated genes relative to the UVB + vehicle group (Fig. 4B). Notably, there were significantly overlapped genes (98) between the downregulated genes in the UVB + vehicle vs. no UVB groups and the upregulated genes in the UVB + h*COL3A1* vs. UVB + vehicle groups ($p = 4.831 \times 10^{-7}$, Fisher's exact test) (Fig. 4C), indicating that h*COL3A1* mRNA treatment particularly and efficiently restores genes suppressed by UVB-induced damage.

Gene set enrichment analysis (GSEA) of Kyoto Encyclopedia of Genes and Genomes (KEGG) pathways revealed that UVB irradiation particularly suppressed many signaling pathways critical for skin homeostasis, including PPAR and TGFβ signaling, as well as pathways related to cell junction integrity and vascular smooth muscle function. Treatment with h*COL3A1* mRNA significantly reversed these pathways toward a more balanced, homeostatic state (Fig. 4D). Similarly, GSEA of Gene Ontology Biological Processes (GOBP) terms demonstrated that UVB exposure inhibited fibroblast, endothelial, and vascular smooth muscle cell proliferation and

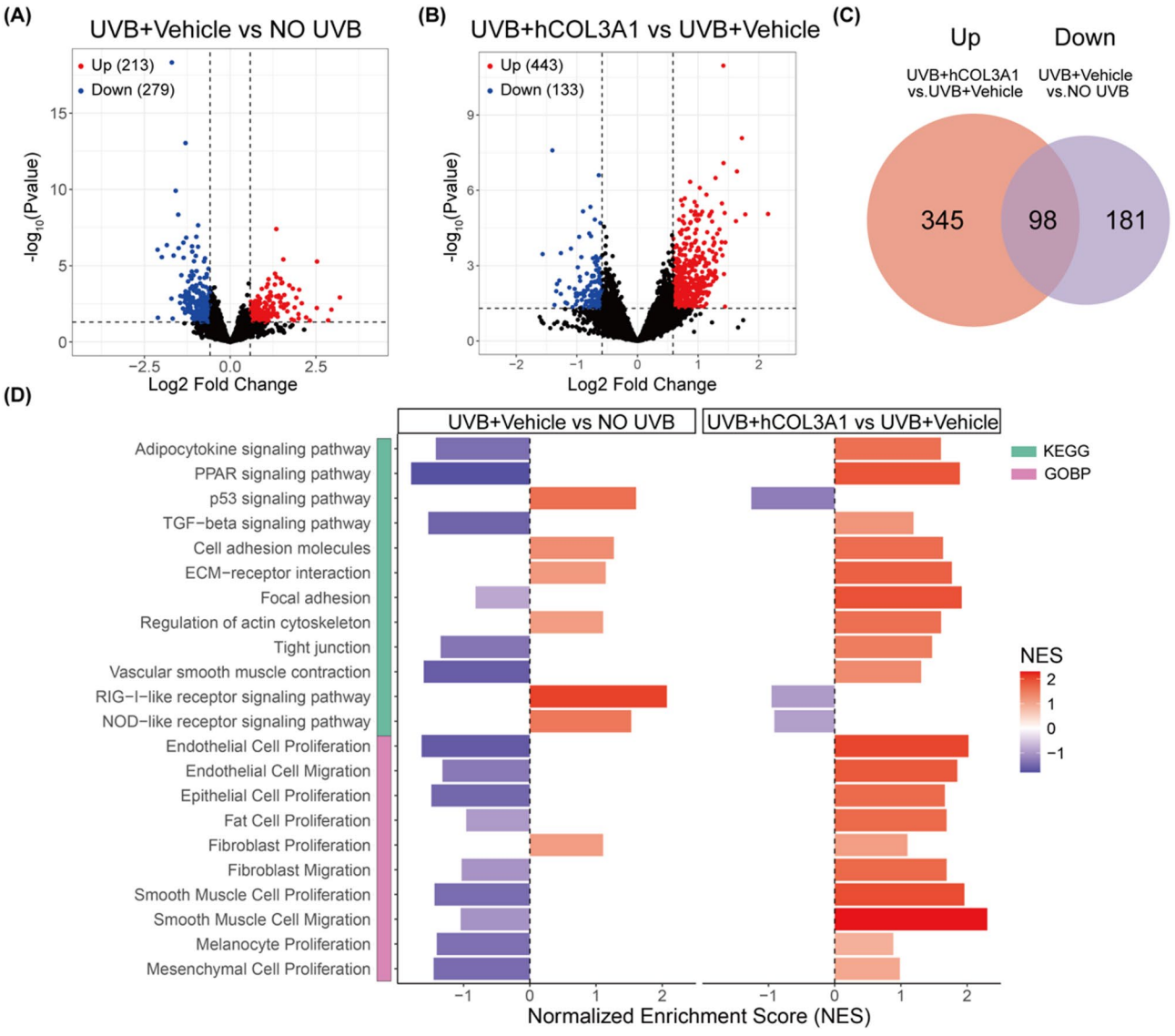

Fig. 4 Transcriptome Analysis of the Protective Effects of h*COL3A1* mRNA. (**A**) Volcano plot illustrating the differential gene expression in dermis tissue between the UVB + vehicle group and the no UVB control group. (**B**) Volcano plot illustrating the differential gene expression in dermis tissue between the UVB + hCOL3A group and the UVB + vehicle group. (**C**) The Venn diagram shows the overlap of genes upregulated in the UVB + h*COL3A1* group vs. the UVB + vehicle group and down-regulated in the UVB + vehicle group vs. the no UVB control group. (**D**) Pathway enrichment analysis of upregulated and downregulated genes in the UVB + vehicle group compared with the no UVB control group and in the UVB + h*COL3A1* mRNA group compared with the UVB + vehicle group

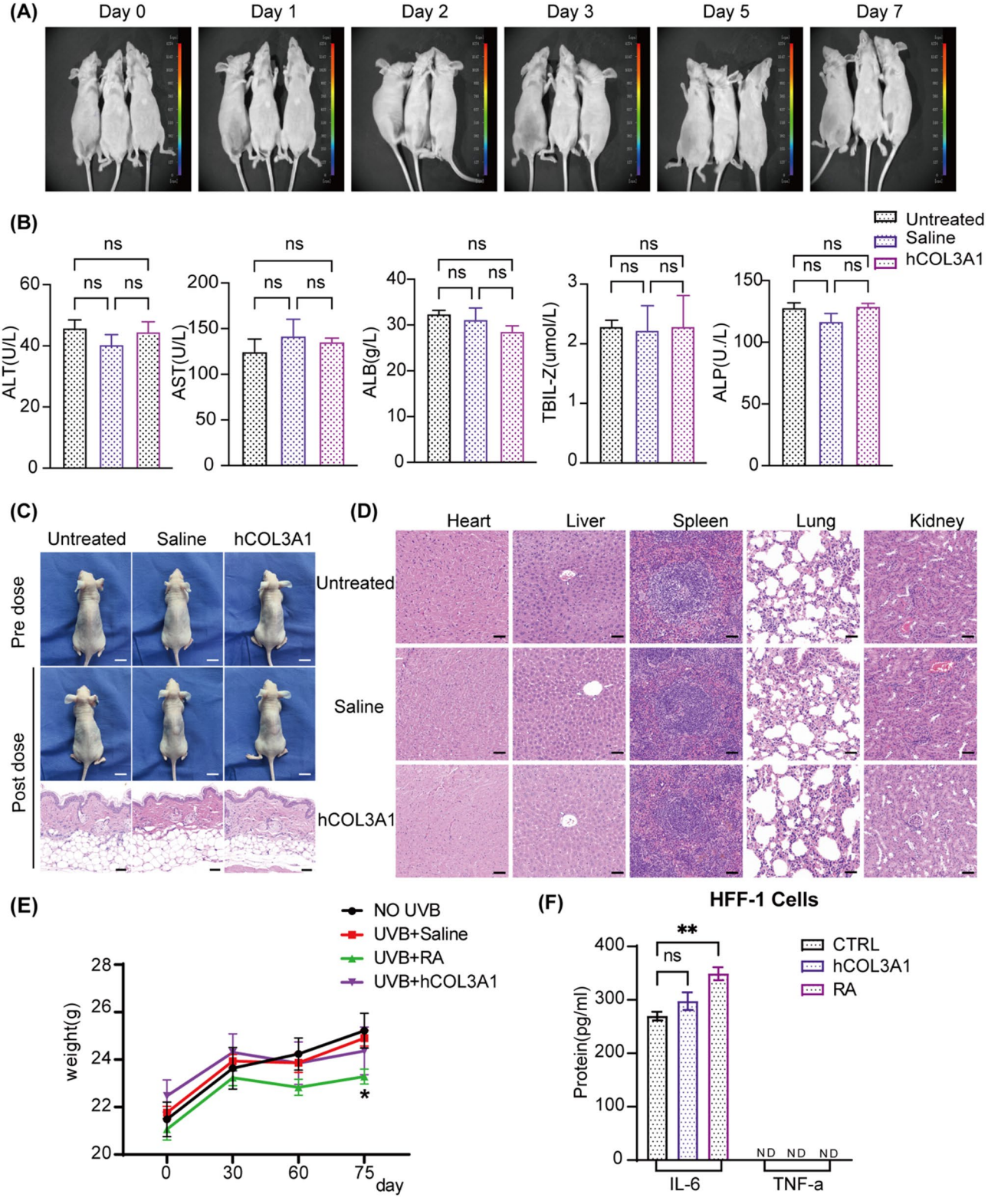

Fig. 5 (See legend on next page.)

(See figure on previous page.)

Fig. 5 Safety Evaluation. (**A**) Representative images showing no detectable Fluc protein expression in the abdominal region around the liver following a 5 μg *FLUC* mRNA-LNP intradermal injection (i.d.) at different time points. (**B**) Hepatic function assessment showing no significant differences between the untreated and treated groups. Data are presented as mean ± SEM ($n = 3$). ALT: alanine transferase; AST: aspartate transferase; ALB: serum albumin; TBIL-Z: total bilirubin; ALP: alkaline phosphatase. (**C**) Representative images showing no significant difference in the dorsal skin between different treatment groups. H&E staining images reveal no noticeable histological changes. Scale bar: 50 μm. (**D**) Representative H&E staining images showing no noticeable histological changes in the heart, liver, spleen, lungs and kidneys between the different groups. Scale bar: 50 μm. (**E**) Quantification of body weight during treatment with UVB irradiation. (**F**) Quantification of IL-6 and TNF-α cytokine release from HFF-1 cells after different treatments following UVB irradiation for 24 h showed no detectable differences. ND: Not Detected. Data are presented as mean ± SEM ($n = 3$). Note: *$p < 0.05$, **$p < 0.01$, ***$p < 0.001$, ****$p < 0.0001$, ns = not significant, determined by one-way analysis of variance (ANOVA)

migration. h*COL3A1* mRNA restored these cellular functions, correlating well with the histological and molecular indicators of improved skin quality observed in our in vitro and in vivo experiments (Fig. 4D). It is also noticeable that cell adhesion molecules, ECM-receptor interaction, and fibroblast proliferation pathways were activated by UVB, which were likely as part of a compensatory response to dermal damage and ECM disruption. Notably, these pathways were further activated by h*COL3A1* mRNA, which enhanced ECM restoration, promoted fibroblast activity, and reinforced cellular adhesion. This suggests that h*COL3A1* mRNA actively stimulates processes essential for skin repair and regeneration.

Additionally, the p53-associated, RIG-I-like receptor and NOD-like receptor signaling pathways were significantly activated by UVB exposure, reflecting a stress-induced inflammatory, immune response and cellular senescence. These pathways were repressed following h*COL3A1* mRNA treatment, showing its role in alleviating UVB-induced cellular senescence, reducing inflammation, and restoring homeostasis in the dermal microenvironment.

In summary, transcriptome analysis validates the protective role of h*COL3A1* mRNA at a molecular level. By restoring key signaling pathways, promoting fibroblast function and improving dermal microenvironment, h*COL3A1* mRNA effectively counters the detrimental transcriptomic alterations induced by UVB irradiation, reinforcing its potential as an innovative therapeutic strategy for photoaged skin.

Safety evaluation of h*COL3A1* mRNA

Given the promising therapeutic outcomes, we finally assessed the safety of h*COL3A1* mRNA delivery, which is crucial to ensure its potential translation into clinical applications as a transformative approach.

After skin injection, LNPs can enter the lymphatic system and subsequently the bloodstream, enabling their distribution to various organs, particularly to the liver, raising considerations for potential off-target effects and safety concerns [21, 53]. We therefore first examined the biodistribution of the injected LNPs. Intradermal injection of *FLUC* mRNA-LNP into the dorsal skin of mice did not result in detectable luciferase expression in the liver over the course of seven days, suggesting that the mRNA remained localized and did not systemically distribute to off-target organs (Fig. 5A). To further assess potential side effects to the liver, we analyzed serum hepatic function indicators, which remained within normal ranges, indicating that h*COL3A1* mRNA-LNP did not affect liver physiology (Fig. 5B).

Repeated intradermal administration of h*COL3A1* mRNA for five times at days 1, 4, 7, 14 and 21 (500ng/each) showed no adverse effects on skin appearance. H&E staining revealed that the treated skin maintained a normal, orderly arrangement without signs of inflammatory infiltration (Fig. 5C). Similarly, histological examinations of major organs, including the heart, liver, spleen, lung, and kidney, detected no pathological abnormalities, confirming the absence of systemic toxicity (Fig. 5D).

Additionally, body weight measurements showed no significant differences between the h*COL3A1* mRNA-treated group and the control group. In contrast, mice treated with RA exhibited a notable decrease in body weight ($p < 0.05$), hinting at systemic side effects associated with RA (Fig. 5E). We also evaluated immunogenicity at the cellular level. While RA treatment significantly increased IL-6 expression ($p < 0.01$), transfection with h*COL3A1* mRNA did not elevate IL-6 levels or TNF-α, suggesting minimal immunostimulatory effects of the mRNA construct (Fig. 5F).

Together, these findings confirmed that intradermal delivery of hCOL3A1 mRNA did not provoke systemic toxicity and elicited no strong immune responses. This safety profile further supports the therapeutic potential of hCOL3A1 mRNA for managing UVB-induced photoaging.

Discussion

In this study, we demonstrated the potential of h*COL3A1* mRNA therapy in treating skin photoaging. By delivering full-length human collagen III mRNA encapsulated in LNPs, we achieved sustained collagen III protein expression and demonstrated significant anti-photoaging effects both in vitro and in vivo.

Unlike conventional protein therapies that rely on animal-derived collagens or recombinant fragments with incomplete structures [20, 54, 55], our approach circumvents difficulties in obtaining high-quality collagen III. By encoding the full-length human *COL3A1* sequence,

the mRNA leverages the host's intrinsic translational and post-translational machinery to produce functional collagen III proteins. The result is a more physiologically relevant and bioactive collagen that can be locally produced in skin cells, potentially reducing the risk of immunogenicity and enhancing therapeutic outcomes [56]. Moreover, mRNA therapeutics offer a transient, non-integrative gene expression modality that avoids insertional mutagenesis concerns and provides a high degree of safety and controllability [57–60]. The flexibility of mRNA sequences and the scalability of manufacturing further position mRNA-based therapies as promising candidates for skincare and regenerative interventions.

Consistent with previous studies demonstrating that collagen III is critical for maintaining dermal fibroblast function and ECM integrity, our in vitro experiments revealed that h*COL3A1* mRNA reduced UVB-induced cellular senescence and apoptosis in HFF-1 fibroblasts. By restoring cell proliferation and promoting migration, h*COL3A1* mRNA preserved the functional capacity of dermal fibroblasts. These findings underscore the importance of collagen III in maintaining ECM integrity, facilitating proper collagen fibril organization, and ensuring the mechanical and biological equilibrium necessary for healthy skin function [61, 62]. Similarly, in vivo studies have reported that collagen III deficiency impairs dermal thickness and ECM organization in mouse skin [17]. Our mouse model of UVB-induced photoaging further confirmed the therapeutic efficacy of h*COL3A1* mRNA. Mice receiving h*COL3A1* mRNA showed improved skin appearance, restored barrier function, increased dermal thickness, and enhanced collagen content. Collagen III levels remained elevated up to 28 days after a single injection, indicating a lasting effect that may reduce the frequency of administration. Additionally, the reduction in senescence markers (p16INK4a and H2A.J) in the skin of treated mice suggested that h*COL3A1* mRNA helps maintain a more youthful cellular environment. Beyond structural improvements, previous reports have shown that UVB exposure activates inflammatory and stress-related pathways, including p53 signaling, while modulating PPAR and TGFβ pathways [63–65]. Our transcriptome analysis is in line with these studies, showing that h*COL3A1* mRNA restored key signaling pathways, including PPAR and TGFβ, while mitigating p53-driven aging signals. By reactivating fibroblast proliferation, migration, and ECM production, h*COL3A1* mRNA addressed the multifaceted pathological landscape of photoaging at a molecular level.

Equally important is the favorable safety profile of h*COL3A1* mRNA with LNPs. No systemic toxicity, organ damage, or significant immune activation was observed following intradermal delivery. The localized and transient nature of mRNA expression, combined with the biocompatibility of LNPs, contributes to this benign safety profile. These attributes are crucial for translating this approach into clinical applications, where long-term safety and patient comfort are critically important.

Our study also highlights the advantages of h*COL3A1* mRNA therapy over RA for the treatment of UVB-induced skin photoaging. While RA is a well-established anti-photoaging agent due to its ability to stimulate collagen synthesis and accelerate cell turnover, its clinical use is hindered by common side effects, including skin irritation, redness, dryness, and increased UV sensitivity [66–68]. In agreement with these previous findings, we observed that RA treatment improved dermal collagen but also cause systemic side effects, such as body weight loss and elevated IL-6 levels. In contrast, h*COL3A1* mRNA did not provoke adverse effects. Our findings further demonstrated that h*COL3A1* mRNA treatment reduced oxidative stress, cellular senescence, and apoptosis as effectively as RA. In addition, h*COL3A1* mRNA therapy effectively restored collagen III levels, improved dermal thickness, and enhanced skin barrier function without inducing inflammation or systemic side effects. The superior efficacy, combined with a more favorable safety profile, positions h*COL3A1* mRNA-LNP as a promising alternative to RA for photoaging therapy, addressing the need for treatments that are both effective and well-tolerated.

Despite the promising results, several limitations warrant attention. First, while our murine model provides valuable insights, human skin differs in structure and complexity. Further studies in large-animal models and eventual human clinical trials are necessary to confirm the translational potential of h*COL3A1* mRNA. Additionally, the optimal dosage, administration frequency, and LNPs formulation require fine-tuning to achieve maximum therapeutic benefit. Investigating synergistic effects with other ECM components or growth factors may further enhance outcomes, as the skin aging process involves multiple interrelated molecular pathways and cellular populations. Long-term follow-up is also needed to determine the durability of benefits, potential need for maintenance therapy, and the interplay of h*COL3A1* mRNA with intrinsic aging factors that evolve over time.

In conclusion, this work positions human collagen III mRNA as a novel and promising therapeutic modality for UVB-induced skin photoaging. By tapping into the body's own protein synthesis machinery, we have established a safer, more adaptable approach that holds the potential which might surpass current protein- or small-molecule-based treatments. Our findings not only lay the groundwork for future clinical translation of mRNA-based dermal therapeutics but also underscore the broader applicability of mRNA technology in regenerative medicine, aesthetic dermatology, and personalized skincare.

Supplementary Information

The online version contains supplementary material available at https://doi.org/10.1186/s12967-025-07351-z.

Supplementary Material 1

Supplementary Material 2

Acknowledgements
We would like to acknowledge the long-term support from Zhongshan Ophthalmic Center, Sun Yat-sen University.

Author contributions
Z.X. conceived and supervised the study. JM.Z. performed experiments in vivo. JM.Z. and SQ.C. performed experiments in vitro. JQ.Y., LF.C. and W.F. made mRNA and LNPs encapsulation. JQ.Y. prepared sequencing libraries. LH.S. performed RNA-seq analysis. R.J. helped interpret experiment results. JM.Z., SQ.C. and Z.X. wrote the manuscript. All authors read and approved the manuscript.

Funding
Funding was provided by National Natural Science Foundation of China (32470705), Key-Area Research and Development Program of Guangdong Province (2023B1111020006), Science and Technology Program of Guangzhou, China (2025A03J3990).

Data availability
All sequencing data have been deposited in the Gene Expression Omnibus (GEO) and will be publicly accessible under an accession number (GSE284483) upon acceptance of the manuscript.

Declarations

Ethical approval
All experiments involving the mice adhered to the procedures outlined in the animal protocols approved by the IACUC at Zhongshan Ophthalmic Center, Sun Yat-Sen University. The animal experimentation ethical number is No. Z2023009.

Consent for publication
All author have reviewed and approved the final version of the manuscript for publication.

Competing interests
The authors declare no competing interests.

Received: 28 March 2025 / Accepted: 21 October 2025
Published online: 13 November 2025

References

1. Farage MA, Miller KW, Elsner P, Maibach HI. Intrinsic and extrinsic factors in skin ageing: A review. Int J Cosmet Sci. 2008;30:87–95.
2. Franco AC, Aveleira C, Cavadas C. Skin senescence: mechanisms and impact on whole-body aging. Trends Mol Med. 2022;28:97–109.
3. Tobin DJ. Introduction to skin aging. J Tissue Viability. 2017;26:37–46.
4. Piao MJ, Hyun YJ, Cho SJ, Kang HK, Yoo ES, Koh YS, et al. An ethanol extract derived from Bonnemaisonia hamifera scavenges ultraviolet B (UVB) Radiation-Induced reactive oxygen species and attenuates UVB-Induced cell damage in human keratinocytes. Mar Drugs. 2012;10:2826–45.
5. Vechtomova YL, Telegina TA, Buglak AA, Kritsky MS. UV radiation in DNA damage and repair involving DNA-photolyases and cryptochromes. Biomedicines. 2021;9.
6. Salminen A, Kaarniranta K, Kauppinen A, Photoaging. UV radiation-induced inflammation and immunosuppression accelerate the aging process in the skin. Inflamm Res. 2022;71:817–31.
7. Chen J, Liu Y, Zhao Z, Qiu J. Oxidative stress in the skin: impact and related protection. Int J Cosmet Sci. 2021;43:495–509.
8. Alafiatayo AA, Lai K-S, Ahmad S, Mahmood M, Shaharuddin NA. RNA-Seq analysis revealed genes associated with UV-induced cell necrosis through MAPK/TNF-α pathways in human dermal fibroblast cells as an inducer of premature Photoaging. Genomics. 2020;112:484–93.
9. Manaloto R, Alster T. Periorbital rejuvenation: A review of dermatologic treatments. Dermatol Surg. 1999;25:1–9.
10. Bucay VW, Day D. Adjunctive skin care of the brow and periorbital region. Clin Plast Surg. 2013;40:225.
11. Narayanan DL, Saladi RN, Fox JL. Ultraviolet radiation and skin cancer. Int J Dermatol. 2010;49:978–86.
12. Feehan RP, Shantz LM. Molecular signaling cascades involved in nonmelanoma skin carcinogenesis. Biochem J. 2016;473:2973–94.
13. Deng M, Xu Y, Yu Z, Wang X, Cai Y, Zheng H, et al. Protective effect of fat extract on uvb-induced Photoaging in vitro and in vivo. Oxidative Med Cell Longev. 2019;2019:6146942.
14. Tracy LE, Minasian RA, Caterson EJ. Extracellular matrix and dermal fibroblast function in the healing wound. Adv Wound Care. 2016;5:119–36.
15. Verzijl N, DeGroot J, Thorpe S, Bank R, Shaw J, Lyons T, et al. Effect of collagen turnover on the accumulation of advanced glycation end products. J Biol Chem. 2000;275:39027–31.
16. Walimbe T, Calve S, Panitch A, Sivasankar MP. Incorporation of types I and III collagen in tunable hyaluronan hydrogels for vocal fold tissue engineering. Acta Biomater. 2019;87:97–107.
17. D'hondt S, Guillemyn B, Syx D, Symoens S, De Rycke R, Vanhoutte L, et al. Type III collagen affects dermal and vascular collagen fibrillogenesis and tissue integrity in a mutant Col3a1 Transgenic mouse model. Matrix Biol. 2018;70:72–83.
18. Nuryana CT, Haryana SM, Wirohadidjojo YW, Arfian N. Achatina fulica mucous improves cell viability and increases collagen deposition in UVB-irradiated human fibroblast culture. J Stem Cells Regenerative Med. 2020;16:26–31.
19. Wang J, Qiu H, Xu Y, Gao Y, Tan P, Zhao R, et al. The biological effect of Recombinant humanized collagen on damaged skin induced by UV-photoaging: an in vivo study. Bioactive Mater. 2022;11:154–65.
20. Ramshaw JAM, Werkmeister JA, Glattauer V. Recent progress with Recombinant collagens produced in Escherichia coli. Curr Opin Biomedical Eng. 2019;10:149–55.
21. Zhang T, Yin H, Li Y, Yang H, Ge K, Zhang J et al. Optimized lipid nanoparticles (LNPs) for organ-selective nucleic acids delivery in vivo. iScience. 2024;27.
22. Wu S, Zhou Y, Yu Y, Zhou X, Du W, Wan M et al. Evaluation of chitosan hydrogel for sustained delivery of VEGF for odontogenic differentiation of dental pulp stem cells. Stem Cells Int. 2019;2019.
23. Liu BXZ, Yu R, Wang J, Wang Z, Harrell C, Randall. The use of type I and type III injectable human collagen for dermal fill: 10 years of clinical experience in China. Semin Plast Surg. 2005;19:241–50.
24. Gothard D, Smith EL, Kanczler JM, Rashidi H, Qutachi O, Henstock J, et al. Tissue engineered bone using select growth factors: a comprehensive review of animal studies and clinical translation studies in man. Eur Cells Mater. 2014;28:166–208.
25. Mukherjee S, Date A, Patravale V, Korting HC, Roeder A, Weindl G. Retinoids in the treatment of skin aging: an overview of clinical efficacy and safety. Clin Interv Aging. 2006;1:327–48.
26. Kang S. Photoaging and tretinoin. Dermatol Clin. 1998;16:357–64.
27. Green LJ, McCormick A, Weinstein GD. Photoaging and the skin. The effects of tretinoin. Dermatol Clin. 1993;11:97–105.
28. Warren L, Manos PD, Ahfeldt T, Loh Y-H, Li H, Lau F, et al. Highly efficient reprogramming to pluripotency and directed differentiation of human cells with synthetic modified mRNA. Cell Stem Cell. 2010;7:618–30.
29. Brand FJ III, Forouzandeh M, Kaur H, Travascio F, Vaccari JP. De R. Acidification changes affect the inflammasome in human nucleus pulposus cells. J Inflamm (Lond). 2016;13.
30. Chen S. Ultrafast one-pass FASTQ data preprocessing, quality control, and deduplication using fastp. iMeta. 2023;2.
31. Langmead B, Salzberg SL. Fast gapped-read alignment with bowtie 2. Nat Methods. 2012;9:357–U54.
32. Dobin A, Davis CA, Schlesinger F, Drenkow J, Zaleski C, Jha S, et al. STAR: ultrafast universal RNA-seq aligner. Bioinformatics. 2013;29:15–21.
33. Li B, Dewey CN. RSEM: accurate transcript quantification from RNA-Seq data with or without a reference genome. BMC Bioinformatics. 2011;12.
34. Love MI, Huber W, Anders S. Moderated Estimation of fold change and dispersion for RNA-seq data with DESeq2. Genome Biol. 2014;15.
35. Subramanian A, Tamayo P, Mootha V, Mukherjee S, Ebert B, Gillette M, et al. Gene set enrichment analysis: A knowledge-based approach for

interpreting genome-wide expression profiles. Proc Natl Acad Sci USA. 2005;102:15545–50.
36. Qu L, Yi Z, Shen Y, Lin L, Chen F, Xu Y, et al. Circular RNA vaccines against SARS-CoV-2 and emerging variants. Cell. 2022;185:1728–.
37. Kimura N, Maeki M, Sato Y, Note Y, Ishida A, Tani H, et al. Development of the Ilinp device: fine tuning the lipid nanoparticle size within 10 Nm for drug delivery. ACS Omega. 2018;3:5044–51.
38. Sato Y, Note Y, Maeki M, Kaji N, Baba Y, Tokeshi M, et al. Elucidation of the physicochemical properties and potency of SiRNA-loaded small-sized lipid nanoparticles for SiRNA delivery. J Controlled Release. 2016;229:48–57.
39. Hassett KJ, Higgins J, Woods A, Levy B, Xia Y, Hsiao CJ, et al. Impact of lipid nanoparticle size on mRNA vaccine immunogenicity. J Controlled Release. 2021;335:237–46.
40. Xu L, Wang X, Liu Y, Yang G, Falconer RJ, Zhao C-X. Lipid nanoparticles for drug delivery. Adv NanoBiomed Res. 2022;2.
41. Laurent GJ. Dynamic state of collagen: pathways of collagen degradation in vivo and their possible role in regulation of collagen mass. Am J Physiol. 1987;252:C1–9.
42. McAnulty RJ, Laurent GJ. Collagen synthesis and degradation in vivo: evidence for rapid rates of collagen turnover with extensive degradation of newly synthesized collagen in tissufes of the adult rat. Collagen Relat Res. 1987;7:93–104.
43. Lin Y, Cao Z, Lyu T, Kong T, Zhang Q, Wu K et al. Single-cell RNA-seq of UVB-irradiated skin reveals landscape of photoaging-related inflammation and protection by vitamin D. Gene. 2022;831.
44. Ascenso A, Ribeiro H, Marques HC, Oliveira H, Santos C, Simoes S. Is tretinoin still a key agent for Photoaging management? Mini-Reviews Med Chem. 2014;14:629–41.
45. de Jager TL, Cockrell AE, Du Plessis SS. Ultraviolet light induced generation of reactive oxygen species. Ultraviolet Light in Human Health, Diseases and Environment. 2017. pp. 15–23.
46. Redza-Dutordoir M, Averill-Bates DA. Activation of apoptosis signalling pathways by reactive oxygen species. Biochim Et Biophys Acta-Molecular Cell Res. 2016;1863:2977–92.
47. Circu ML, Aw TY. Reactive oxygen species, cellular redox systems, and apoptosis. Free Radic Biol Med. 2010;48:749–62.
48. Wang B, Wang Y, Zhang J, Hu C, Jiang J, Li Y, et al. ROS-induced lipid peroxidation modulates cell death outcome: mechanisms behind apoptosis, autophagy, and ferroptosis. Arch Toxicol. 2023;97:1439–51.
49. De Cecco M, Ito T, Petrashen AP, Elias AE, Skvir NJ, Criscione SW, et al. L1 drives IFN in senescent cells and promotes age-associated inflammation. Nature. 2019;572:E5–5.
50. Yoshimura T, Manabe C, Inokuchi Y, Mutou C, Nagahama T, Murakami S. Protective effect of taurine on UVB-induced skin aging in hairless mice. Biomed Pharmacother. 2021;141.
51. Zonari A, Brace LEE, Al-Katib K, Porto WFF, Foyt D, Guiang M et al. Senotherapeutic peptide treatment reduces biological age and senescence burden in human skin models. NPJ Aging. 2023;9.
52. Ruebe CE, Baeumert C, Schuler N, Isermann A, Schmal Z, Glanemann M et al. Human skin aging is associated with increased expression of the histone variant H2A.J in the epidermis. NPJ Aging Mech Disease. 2021;7.
53. Wang J, Ding Y, Chong K, Cui M, Cao Z, Tang C et al. Recent advances in lipid nanoparticles and their safety concerns for mRNA delivery. Vaccines. 2024;12.
54. Hua C, Zhu Y, Xu W, Ye S, Zhang R, Lu L, et al. Characterization by high-resolution crystal structure analysis of a triple-helix region of human collagen type III with potent cell adhesion activity. Biochem Biophys Res Commun. 2019;508:1018–23.
55. Aly N, Benoit E, Chaubard J-L, Chintalapudi K, Choung S, de Leeuw M et al. Cosmetic potential of a recombinant 50 kDa protein. Cosmetics. 2022;9.
56. Wolkow N, Jakobiec FA, Dryja TP, Lefebvre DR. Mild complications or unusual persistence of Porcine collagen and hyaluronic add gel following periocular filler injections. Ophthal Plast Reconstr Surg. 2018;34:E143–6.
57. Tavernier G, Andries O, Demeester J, Sanders NN, De Smedt SC, Rejman J. mRNA as gene therapeutic: how to control protein expression. J Controlled Release. 2011;150:238–47.
58. Jiang W, Xiao D, Wu C, Yang J, Peng X, Chen L et al. Circular RNA-based therapy provides sustained and robust neuroprotection for retinal ganglion cells. Mol Therapy Nucleic Acids. 2024;35.
59. Sahin U, Kariko K, Tuereci O. mRNA-based therapeutics - developing a new class of drugs. Nat Rev Drug Discovery. 2014;13:759–80.
60. Pardi N, Hogan MJ, Porter FW, Weissman D. mRNA vaccines - a new era in vaccinology. Nat Rev Drug Discovery. 2018;17:261–79.
61. Asgari M, Latifi N, Heris HK, Vali H, Mongeau L. In vitro fibrillogenesis of tropocollagen type III in collagen type I affects its relative fibrillar topology and mechanics. Sci Rep. 2017;7.
62. Stuart K, Panitch A. Characterization of gels composed of blends of collagen I, collagen III, and chondroitin sulfate. Biomacromolecules. 2009;10:25–31.
63. Wen S-Y, Ng S-C, Chiu Y-T, Tai P-Y, Chen T-J, Chen C-J, et al. Enhanced SIRT1 activity by galangin mitigates UVB-induced senescence in dermal fibroblasts via p53 acetylation regulation and activation. J Agric Food Chem. United States; 2024;72:23286–94. /acs.jafc.4c05945.
64. Ham SA, Kang ES, Lee H, Hwang JS, Yoo T, Paek KS, et al. PPARδ inhibits UVB-induced secretion of MMP-1 through MKP-7-mediated suppression of JNK signaling. J Invest Dermatol United States. 2013;133:2593–600.
65. Ke Y, Wang X-J. TGFβ signaling in Photoaging and UV-Induced skin cancer. J Invest Dermatol United States. 2021;141:1104–10.
66. Siddiqui Z, Zufall A, Nash M, Rao D, Hirani R, Russo M. Comparing tretinoin to other topical therapies in the treatment of skin photoaging: a systematic review. Am J Clin Dermatol. 2024;25:873–90.
67. Buccitelli C, Selbach M. mRNAs, proteins and the emerging principles of gene expression control. Nat Rev Genet. 2020;21:630–44.
68. Paunovska K, Loughrey D, Dahlman JE. Drug delivery systems for RNA therapeutics. Nat Rev Genet. 2022;23:265–80.

Publisher's note